Low Reynolds Number Flow Dynamics of a Thin Airfoil with an Actuated Leading Edge

Kevin J. Drost*   Heather Johnson*   Sourabh V. Apte†

James A. Liburdy‡

School of Mechanical Industrial and Manufacturing Engineering, Oregon State University, Corvallis, OR 97331

Use of oscillatory actuation of the leading edge of a thin, flat, rigid airfoil, as a potential mechanism for control or improved performance of a micro-air vehicle (MAV), was investigated by performing direct numerical simulations and experimental measurements at low Reynolds numbers. The leading edge of the airfoil is hinged at 30% of the chord length allowing dynamic variations in the effective angle of attack through specified oscillations (flapping). This leading edge actuation results in transient variations in the effective camber and angle of attack that can be used to alleviate the strength of the leading edge vortex at high angles of attack. A fictitious-domain based finite volume approach [Apte et al., JCP 2009] was used to compute the moving boundary problem on a fixed background mesh. The flow solver is three-dimensional, parallel, second-order accurate, capable of using structured or arbitrarily shaped unstructured meshes and has been validated for a range of canonical test cases including flow over cylinder and sphere at different Reynolds numbers, and flow-induced by inline oscillation of a cylinder, as well as flow over a plunging SD7003 airfoil at two Reynolds numbers (1000 and 10,000).

To assess the effect of an actuated leading edge on the flow field and aerodynamic loads, parametric studies were performed on a thin, flat airfoil at 20 degrees angle of attack at low Reynolds number of 14,700 (based on the chord length) using the DNS studies; whereas, wind-tunnel measurements were conducted at higher Reynolds number of 42,000. The actuator was dynamically moved by sinusoidally oscillating around the hinge over a range of reduced frequencies (k=0.57-11.4) and actuation amplitudes. It was found that high-frequency, low-amplitude actuation of the leading edge significantly alters the leading edge boundary-layer and vortex shedding and increases the mean lift-to-drag ratio. This study indicates that the concept of an actuated leading-edge has potential for development of control techniques to stabilize and maneuver MAVs at low Reynolds numbers.

Nomenclature

ℓ_a	Leading edge actuator length, m
c	Chord length, m
θ	Actuator angle, degree
$\Delta\theta$	Actuation amplitude, degree
f	Actuation frequency, Hertz
α	Angle of attack, degree
α_{eff}	Effective angle of attack, degree
Re	Reynolds number
C_D	Drag coefficient
C_L	Lift coefficient
k	Reduced frequency

*Graduate Student, Mechanical Engineering, Corvallis OR 97331, and Student Member.

†Corresponding Author, Assistant Professor, Mechanical Engineering, 308 Rogers Hall, Corvallis OR 97331, Email: sva@engr.orst.edu.

‡James R. Welty Chaired Professor of Fluid Mechanics, Mechanical Engineering, 310 Rogers Hall, Corvallis OR 97331.

American Institute of Aeronautics and Astronautics

Subscript
D Drag
L Lift
a Actuator
eff   Effective

I.   Introduction

The desire to advance the use of thin, low Re wings at small scales introduces flow dynamics that significantly influence their performance and flow control. At sufficiently high angles of attack during transients, flow over an airfoil separates, which can lead to a 'dynamic stall' condition. Dynamic stall, identified by an abrupt change of lift for airfoils in motion and undergoing maneuvers, plays a crucial role in developing a control mechanism to maintain large lift-to-drag ratios for thin airfoils. Solutions to this problem will have a variety of applications ranging from newly emerging micro air vehicle (MAV) development to hydrofoils, sails, stabilizers, as well as rotary or flapping wing development.

The primary objective of the proposed work is to investigate the potential benefits to the lift and drag characteristics of a flapping leading edge on thin, flat airfoils at low Reynolds numbers [$\mathcal{O}(10^4)$] with and without pitching maneuvers. In this work, high-fidelity direct numerical simulations (DNS) as well as experimental lift and drag measurements on a thin, flat wing are used to understand the effects of a *movable front actuator* on the leading edge vortex shedding, separation bubble dynamics and dynamic stall conditions. This work focusses on a fixed wing concept in which a leading edge actuator is utilized to achieve a weaker separation bubble by conditioning the leading edge boundary layer development during maneuvers (see Figure 1). A thin, flat wing with a movable front actuator is chosen, since (i) thin airfoil design

Figure 1.   **Schematic of a thin, flat airfoil with a leading edge actuator. An actuator of length (ℓ_a) approximately 30% of the chord (c) is hinged to the airfoil body to facilitate change in actuator angle (θ) and the angle of attack (α).**

has been shown to provide adequate lift conditions for many possible applications, (ii) the leading edge instability resulting in unsteady, dynamic stall conditions occurs for this design as well as other more complex airfoils, (iii) a movable front actuator provides a means to directly influence the leading edge stall condition and unsteady lift behavior while not adding complexities associated with blowing or suction that may not be practical, for small wings with weight constraints.

As the first step, the chief aim in this work is to parameterize the flow field and vortex dynamics over a range of angles of attack and flap angle for a fixed flap-length to chord ratio at low Reynolds numbers under steady flow conditions representative of micro-air vehicle operation. The *central hypotheses* driving this work are:

- A movable leading edge actuator provides an effective mechanism to control transients in lift, drag, and pitching moment during steady and transient flow conditions at low Reynolds numbers [$\mathcal{O}(10^4)$] by reducing the strength of the generated vortex and weakening the separation bubble;

- Actuation time scales and waveforms associated with the actuator motion can *positively* influence the lift characteristics by altering the leading-edge vortex shedding, separation-bubble dynamics, and dynamic stall conditions.

The leading edge actuator concept provides (i) camber and a static form modifying the leading edge vortex, and (ii) a dynamic effect when the leading edge is flapped or actuated. The latter is of critical importance as recent numerical studies at AFRL[1,2] on low Re plunging airfoils indicate that plunging motion significantly alters the dynamic stall vortex by breaking down the vortex as it plunges against the airfoil surface. High-frequency small-amplitude plunging oscillations of stalled airfoil resulted in elimination
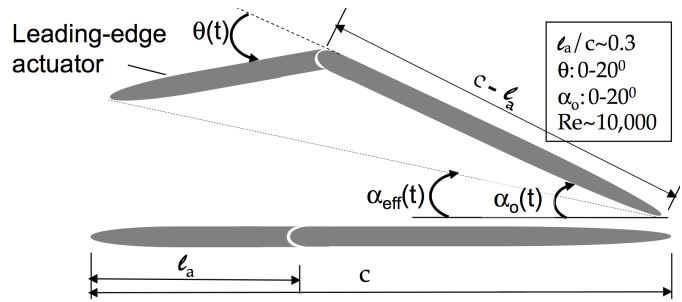
American Institute of Aeronautics and Astronautics

of coherent vortex structures propagating along the airfoil surface. The proposed leading edge actuator mechanism can essentially provide similar modification of the leading edge vortex. Modulating the angular position of the leading edge actuator, one can modify the effective angle of attack to provide improved stability under airfoil maneuvers. Control strategies based on the above mentioned leading edge actuator are of direct relevance to small-size MAVs undergoing maneuvers and are pragmatic as designing simple piezo-based actuators is straightforward. It is thus crucial to investigate the flow dynamics of the thin airfoil in the presence of an actuator to exploit its potential benefits in designing control strategies. If successful, this simple modification to the wing configuration also facilitates development of actuators and controllers for airfoils with considerable size and weight restrictions. For instance, typical characteristic lengths for MAV are in the range of 8–15 cm, with operating speeds on the order of 50 km/h. Improving the flight performance of these vehicles can enhance surveillance, search and rescue, and sensor mobility, while yielding vehicles that are more disposable.

In this work, direct numerical simulations are performed to investigate the influence of the leading edge actuation on lift and drag characteristics of high aspect ratio (two-dimensional) wings at a Reynolds number of $[\mathcal{O}(10^4)]$ with a fixed actuator-length to chord ratio of 0.3. The high aspect ratio wing is selected in order to isolate the effect of the leading edge actuator and not complicate the flow dynamics by tip-vortex interactions, which may be important in some applications. The range of parameters to be considered ($\alpha = 0^0$–20^0, and $\theta = 0^0$–20^0, $Re = 10^4$–7×10^4) are of direct relevance to the design of unmanned micro-air vehicles at low Reynolds numbers. Flow parameterization is performed under *steady* upstream flow conditions. The numerical simulations need handling of complex moving boundaries to capture the motion of the actuator. This is accomplished by using a fictitious domain based numerical approach developed by Apte *et al.*[3] This approach is similar to immersed boundary methods and allows simulations of moving boundaries on a fixed grid. This approach has been implemented into a second-order, co-located grid finite-volume solver.[4] Testing and validation of the approach for flow over thin airfoils is conducted by comparing results with high-fidelity approaches using higher-order immersed boundary methods.

After detailed validation of the numerics as applied to plunging airfoils, effect of variations in the actuator angles ($\dot{\theta}$) on the coefficients of lift and drag are obtained for a fixed angle of attack (α); i.e. ($\mathcal{C}_L, \mathcal{C}_D = \mathcal{G}(\theta, \dot{\theta}, t)$). In order to validate the numerical findings, an experimental setup with actuated leading edge is developed in a wind tunnel allowing detailed lift and drag measurements. In this proof-of-concept study, the numerical simulations are typically restricted to low Reynolds numbers (~ 10000), owing to the two-dimensionality assumption as well as large grid and computing time requirement. Experimental data, on the other hand, shows low uncertainty and noise at the higher range of low Reynolds number studies (40000–70000).

The paper is arranged as follows. A detailed review and background on past relevant work is discussed in section (II). Details of the computational approach as well as experimental setup are described in section (III). Verification and validation studies of the numerical approach as applied to SD7003 airfoil are discussed next in the results section (IV). Parametric studies varying the actuation frequency and amplitude at low Reynolds numbers (using DNS) and higher Reynolds numbers using (experimental data) are documented next. Finally, the results and conclusions are summarized in section (V).

II.   Background

One major concern of thin airfoil design, when operating at high lift and stall conditions, is the unsteady nature of separation at the leading edge resulting in a Kelvin-Helmhotlz type flow instability.[5–7] This causes the generation and convection of low frequency large vortical structures that have a strong influence on unsteady lift. Very early works on flow over hydrofoils and wings[8,9] have shown a strong correlation of pressure in the separation bubble with the onset of stall conditions.

There has been fairly extensive work, both experimental and computational, on flow separation and control for thin airfoils at moderate-to-high Reynolds numbers ($Re \geq 10^5$).[7,10–12] A critical angle of attack exists for the occurrence of dynamic stall.[11] Separation of the turbulent boundary layer typically is spread, in time and space, and involves a spectrum of states. By mapping the separation into incipient, transitory, and complete detachment,[13] the unsteady properties of the separation zone, including the oscillation of the length of the separation region, have been correlated with the surface pressure.[7] Application of suction near the leading edge has been shown to delay flow separation and inhibit dynamic stall on thin airfoils.[10] Direct numerical studies[14,15] on flow over cylinders have shown considerable reduction in lift variation by

American Institute of Aeronautics and Astronautics

using suction to control the vortex shedding. There is a large literature dealing with pulsed and synthetic jets,[16–20] plasma discharge based actuation[21–26] for flow control applications resulting in increased lift-to-drag ratio.

For *very low Re* [$\mathcal{O}(100)$], the unsteady flow characteristics of thin wings undergoing plunge maneuvers show downstream advection of the leading edge vortex and resultant unsteady lift.[27] Other studies during pitching[28–31] and recent computational work based on immersed boundary technique at CalTech on an impulsively started wing[32–34] show that vortex shedding, advection, and strength is highly dependent on the maneuvering characteristics.

Extensive studies at *low Re* [$\mathcal{O}(10^2 - 10^5)$] have been carried out to better understand the flow dynamic characteristics for stability and control considerations, including pitching and heaving airfoils. The character of laminar separation, transition and dynamic stall through simulations indicate the role of vortex generation, separation bubble turbulence generation during heaving and that a time averaged laminar separation bubble reacts to changing angle of attack.[1,2] At low Re the separation bubble growth increases drag. Corresponding experimental studies using the same airfoil[35,36] provide details of the separation bubble during plunging and its effects on transition. Pitching and plunging has been the focus of low Reynolds number flight[37,38] with emphasis on vortex development. Simulations of plunging have also found that vortex advection during dynamic stall can be greatly influenced by plunge conditions.[1]

Thin flat airfoils actually *delay* stall to higher angles of attack when operating at low Re and low aspect ratios, although the lift is smaller at lower angles of attack.[39] It has been shown that a cambered plate (4%) performs better for Re of 10^4–10^5,[39] and has a low sensitivity to the trailing edge geometry and turbulence intensities.[40] Although thin airfoils show many advantages at low Re, such as high lift-to-drag ratio, they exhibit *wide fluctuations in lift* mainly caused by the unsteady flow separation at the leading edge ([41] and references therein). The character of this separation is highly unsteady, at fairly low frequencies, and without reattachment if the angle of attack is sufficiently large.[41] However, most of this work is at comparatively larger Re ($\sim 3 \times 10^5$). As the angle of attack is increased to the stall condition there is a rise in the unsteady character of the lift coefficient, with normalized *rms* fluctuations on the order of 0.1–0.2. This is in contrast to the unsteady lift coefficients which are on the order of 0.03 for trailing edge stall. The thin airfoil stall versus increasing angle of attack is associated with a drop in lift coefficient, a rise in unsteadiness and a subsequent rise in lift, and it is asserted that the unsteadiness in lift is a direct consequence of the leading edge separation.[41] Effect of impressed acoustic excitation of the airfoil as a method of flow control[42] has been investigated to reduce the unsteadiness in lift oscillations. Vorticity mapping, to quantify unsteady flow associated with airfoil motion, has been used to correlate thrust with shedding frequency.[43]

For low Re conditions, high lift could be obtained by applying a concave pressure recovery and aft loading,[44] using flexible airfoils,[45] and/or using boundary layer trips with transition ramps[46] leading to further improvements in lift-to-drag ratios. Consistent with these observations, it has been shown that thin airfoils can be optimized at *ultra-low* Reynolds numbers ($Re \sim 10^3$) by modifying the leading edge shapes and conditions. Airfoil shapes with a 'droop' near the leading edge provide an increase in effective camber and result in improved lift-to-drag ratios (greater than 16%).[47] This may be a result of reducing the leading edge instability and strongly points to the potential advantages of using a leading edge actuator for control purposes.

III.   Methodology

In this section, brief descriptions of the computational and experimental methodologies are provided.

A.   Computational Approach

The computational algorithm for flow over immersed objects on simple Cartesian grids is based on a fictitious domain approach.[3,48] In this approach, the entire fluid-rigid body domain is assumed to be an incompressible, but variable density, fluid. The flow inside the fluid region is constrained to be divergence-free for an incompressible fluid, whereas the flow inside the particle (or rigid body) domain is constrained to undergo rigid body motion (i.e. involving translation and rotational motions only). For specified motion of the rigid body, the rigidity constraint force can be readily obtained once the location of the boundary of the rigid body is identified by making use of Lagrangian marker points (LP) in a banded region surrounding the rigid body surface (figure 2). The marker points provide subgrid scale resolution, improving the accuracy

of interpolations between the Lagrangian points and the background grid. Due to rigidity of the moving object, there is no relative motion between the marker points, and all points move with the same, specified velocity field. The rigidity constaint force is then enforced in a standard fractional step scheme. The basics of the computational algorithm are given below; for details refer to Apte *et al.*[3, 48]

The momentum equations together with the incompressibility constraint are:

$$\frac{\partial u_j}{\partial x_j} = 0; \qquad \frac{\partial u_i}{\partial t} + \frac{\partial u_j u_i}{\partial x_j} = -\frac{1}{\rho}\frac{\partial p}{\partial x_i} + \frac{1}{\rho}\frac{\partial \tau_{ij}}{\partial x_j} + g_i + \frac{1}{\rho}F_{R,i} \tag{1}$$

where τ_{ij} is the viscous stress tensor, and $F_{R,i}$ is the rigidity constraint force *that is present only inside the particle region* to enforce the rigid body motion. These equations are solved using a *three-level fractional step algorithm.* First, the momentum equations are solved, using symmetric, energy conserving discretization.[49] The incompressibility constraint is then imposed by solving a pressure Poisson equation (obtained by taking the divergence of the momentum equation). The algorithm uses symmetric, central differencing for momentum fluxes and eliminates the need for any upwind biased stencil for stability. Since rigid objects do not deform, mass of the two phases are conserved and it has been shown that this scheme has good conservation properties necessary for *turbulent flow simulations.*[3, 48]

The resultant velocity field can be decomposed into a rigid body component ($\mathbf{u}^{RBM}$) and a deformational component ($\mathbf{u}'$); $\mathbf{u} = \mathbf{u}^{RBM} + \mathbf{u}'$, where $\mathbf{u}^{RBM} = \mathbf{U}_p^T + \mathbf{\Omega}_p \times \mathbf{r}$, *RBM* stands for rigid body motion consisting of translational ($\mathbf{U}_p^T$) and rotational components, $\mathbf{\Omega}_p$ is the angular rotation rate, and $\mathbf{r}$ is the position vector of an LP with respect to the immersed object centroid. The *RBM* and rigidity constraint force can be obtained by requiring $\bigtriangledown \cdot \left(\mathbf{D}[\mathbf{u}^{n+1}]\right) = 0$ in P(t) and $\mathbf{D}[\mathbf{u}^{n+1}] \cdot \mathbf{n} = 0$ on ∂P(t). Here, P(t) is the region of the background grid occupied by the object, ∂P(t) the boundary of the immersed object, $\mathbf{D}[u^{n+1}]$ is the symmetric part of the velocity gradient field and $\mathbf{n}$ is the unit outward normal on the object surface. The deformation-rate tensor is constrained to be zero making the motion of the region within rigid domain a RBM. In the present simulations, the rigid body motion of the immersed object is *specified* and thus $\mathbf{U}_p^T$ and $\mathbf{\Omega}_p$ are completely known at each time-step. This gives the rigid body motion and rigidity constraint force (non-zero only inside the immersed object) as:

Figure 2. Use of banded marker points to identify the rigid body surface in a fictitious-domain approach.[3, 50]

$$\mathbf{F}_R = -\rho_p \mathbf{u}'/\Delta t. \tag{2}$$

The above approach has been implemented in a fully parallel and conservative finite-volume scheme[4] for accurate prediction of turbulent flows and has been verified on a variety of canonical test cases such as flow over a cylinder, sphere and a NACA airfoil to show good predictive capability.[3, 50] In order to verify the solver and also assess its predictive capability as applied to flow over airfoils over a range of Reynolds numbers $[\mathcal{O}(10^2 - 10^5)]$, relevant to the operating conditions of micro-air vehicles, a systematic grid refinement study was performed on a standard test case of flow over SD7003 airfoil. The results are also compared with AFRL's very high-fidelity solver FDL3DI developed by Visbal and co-workers[1, 2] and are given below.

B. Experimental Approach

A motor-controlled two-dimensional wing with an actuated leading edge that can be mounted on a sting balance has been designed for the typical operating conditions of low-*Re* wings ($\alpha_0 = 0°$–$20°$, and $\theta = 0°$–$20°$, and tested in the wind tunnel at OSU (figure 3a). A test rig has also been built for wind-tunnel experiments with simultaneous pitching of the airfoil and flapping of the leading edge. The wind tunnel experiments facilitate accurate lift and drag measurements, flow visualization studies and validation data, especially at higher Reynolds numbers of 40000–70000.

The experimental studies were carried out in the low speed recirculating wind tunnel (1.2 m × 1.4 m) at Oregon State University with turbulence levels under 1.0%. For measurement of the lift, drag, and pitching moment, the wind tunnel is equipped with a Aerolab six component strain gage sting balance with 0.01 lb
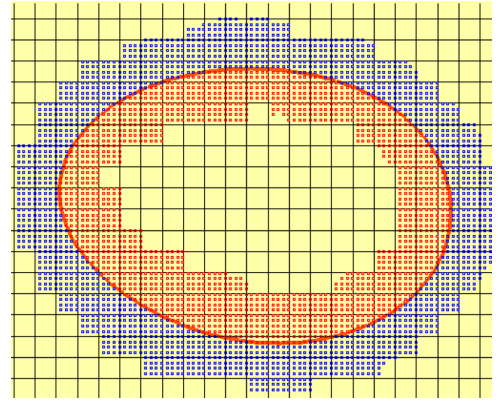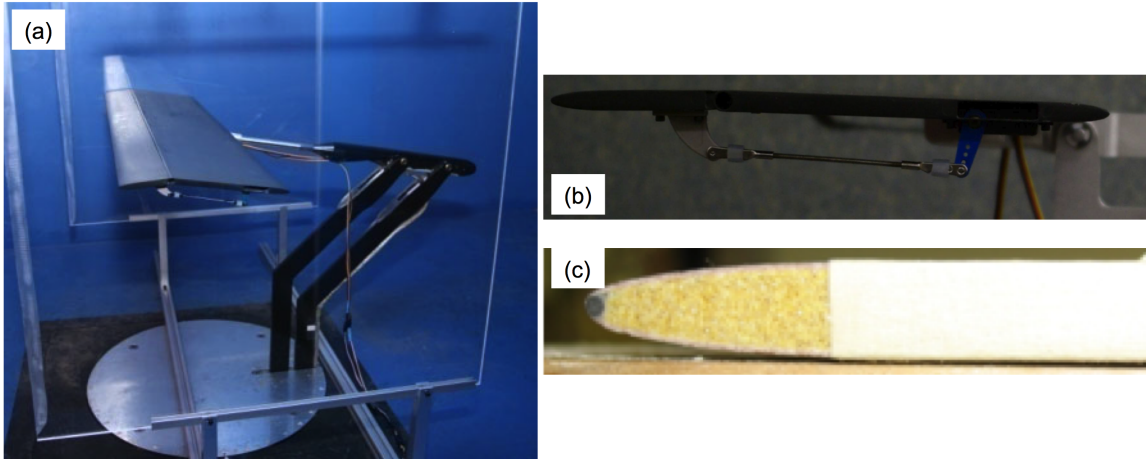
Figure 3. Airfoil setup: (a) photograph of the wing mounted in the wind tunnel, (b) side view of the wing showing the flapping mechanism for the leading edge actuator, (c) close-up of the elliptical leading edge.

resolution, maximum 10 lb load and 15 in-lb pitching moment. The system has been reconfigured to collect data at 1 kHz for transient data analysis (although the present data are collected at 300 Hz). The wing used in the experimental studies has a chord length of 20 cm and span of 77 cm and was fabricated from a 6.3 mm thick Divinycell HT110 core between two 0.6 mm thick carbon fiber sheets. The leading and trailing edges use a 1.5 mm rod to form, through proper sanding of the wing core and surface material, a 1:5 elliptic edge. A leading edge actuator forms the front 30% of the total chord length which can rotate about a 8 mm diameter fiberglass tube with Robart hinges which provide a smooth transition between the actuator and wing surface. For these studies the wing is held stationary at a prescribed angle of attack while the leading edge actuator is controlled through a servo-motor system capable of providing an actuator angle from 30° down to 12° up as measured relative to the chord line. Oscillations can be obtained up to 5 Hz using a prescribed input waveform. The data presented used a sine wave with $\Delta\theta = \pm5°$ amplitude centered about the horizontal position. Side plates were positioned along the wing tips to help eliminate any tip effects.

To understand the impact of the actuator performance, a regime map based on experimental measurements of $\mathcal{C}_L, \mathcal{C}_D = \mathcal{F}(\alpha, \theta, t)$ is first obtained under steady flow conditions (no actuation). For certain high angles of attack, the lift force on an airfoil varies with time owing to the dynamics of vortex shedding and leading edge separation. The flow characteristics at the leading edge of a thin, flat, low aspect ratio wing at relatively high angles involving flow separation, vortex generation, and vortex convection have been studied by the authors in the past at various angles of attack (15°-20°) using a three-component, time-resolved PIV.[51–55] This study was performed for a static wing without any actuation (i.e. $\theta = 0$).

Static results (i.e. the actuator is not activated, but is held stationary at different angles relative to the angle of attack) of lift for varying actuator angle and angle of attack are shown in figure 4. For large angles of attack, there exists an actuator angle, that increases with increasing angle of attack, yielding the maximum lift force. This suggests possibilities of a novel control strategy using the leading actuator for improved lift and stability of a thin airfoil undergoing maneuvers. In the present study, for an angle of attack of 20°, the mean actuator angle was kept at $\theta = 20°$ for static as well as dynamic actuation. This configuration is close to the optimal position for high lift based on the data shown in figure 4.

IV. Results

This section is arranged as follows. First, the computational studies involving verification tests as well as grid refinement studies on a SD7003 plunging airfoil and comparisons to the work by Visbal and co-workers[1, 2] are present. Next, validation and parametric studies of leading edge actuation for a thin, flat airfoil are presented in two parts. First, a static actuation test is considered wherein the actuator is held stationary at an optimal actuation attack relative to the angle of attack. Validation data comparing lift coefficients with available experimental data is also presented. Dynamic actuations with prescribed sinusoidal oscillations of
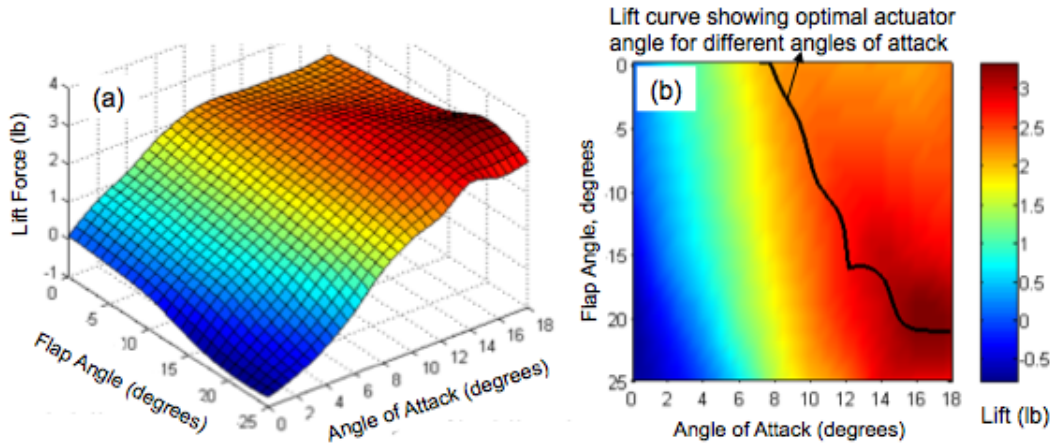
Figure 4. Lift versus angle of attack (α) and actuator (or flap) angle (θ) indicating existence of an optimal actuator angle for large angles of attack at $Re = 70,000$: (a) surface map, (b) contour map showing optimal actuator angle for a given angle of attack.

the actuator at different frequencies and amplitudes around the mean actuator position are presented next for $Re = 14700$. Finally, experimental data with dynamic actuation of the leading edge is presented for higher Reynolds number of $Re = 42000$.

A.   Verification Tests

The fictitious-domain approach was used to simulate flow over a plunging SD7003 airfoil, corresponding to the high-fildeity simulations by Visbal.[1,2] This configuration has also been a subject of several experimental and numerical studies.[37] The case with chord Reynolds numbers of 10^3 and 10^4 were investigated. This test case is crucial to establish predictive capability of the present solver compared to AFRL's high-fidelity FDL3DI solver. In addition, it also allows to establish minimum grid resolution requirements to obtain grid converged results for flat airfoils studied next. This airfoil has a maximum thickness of 8.5% and a maximum camber of 1.45% at 35% chord length. The original sharp trailing edge was rounded with a circular arc of radius ($r/c \approx 0.0004$, c is the chord length) corresponding to the simulations by Visbal.[2] The flow conditions correspond to angle of attack (α) of 4°, non-dimensional plunge amplitude $h_0 = h/c = 0.05$, reduced frequency of plunging motion, $k = \pi f c/U_\infty = 3.93$, where U_∞ is the free-stream velocity. A ramp function was used to allow smooth transition to the periodic plunging motion:

$$h(t) = h_0 \sin[2kF(t)t]; \quad F(t) = 1 - e^{-at}; \quad a = 4.6/t_0; \quad t_0 = 0.5. \tag{3}$$

Table 1.   Grid and time-step resolutions for the SD7003 case used in present study (first three rows) and computations by Visbal and co-workers[2] (bottom two rows).

Grid	$\Delta x/c$ (or $\Delta s/c$)	$\Delta y/c$ (or $\Delta n/c$)	$\Delta t U_\infty/c$
Baseline	0.00275	0.00275	0.0002
Coarse	0.005	0.005	0.0004
Non-uniform	0.005	0.0008	0.0002
Baseline[2]	0.005	0.00005	0.00005
Coarse[2]	0.01	0.001	0.0001

The grid resolution and time-step used for the present study are given in Table 1. A simple Cartesian grid refined in a small patch around the airfoil was used. Two grid points were used in the spanwise direction, with periodic conditions, for this two-dimensional study. Visbal[2] used a body-fitted, moving grid, and a sixth-order accurate algorithm with wall-normal resolution of 0.00005 and 0.0001 (non-dimensionalized by chord
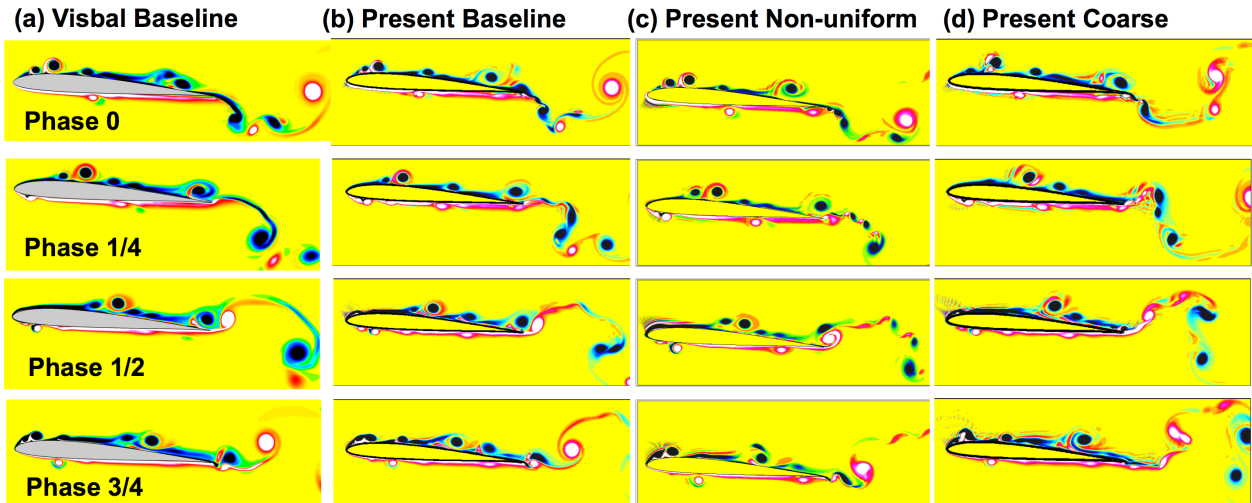
American Institute of Aeronautics and Astronautics

Figure 5. Instantaneous, out-of-plane vorticity contours ($\omega_z c/U_\infty$, range ± 40) for $Re = 10,000$: (a) results by Visbal[2] on their baseline grid, (b) present results on baseline grid, (c) present results on non-uniform grid, and (d) present results on coarse grid.
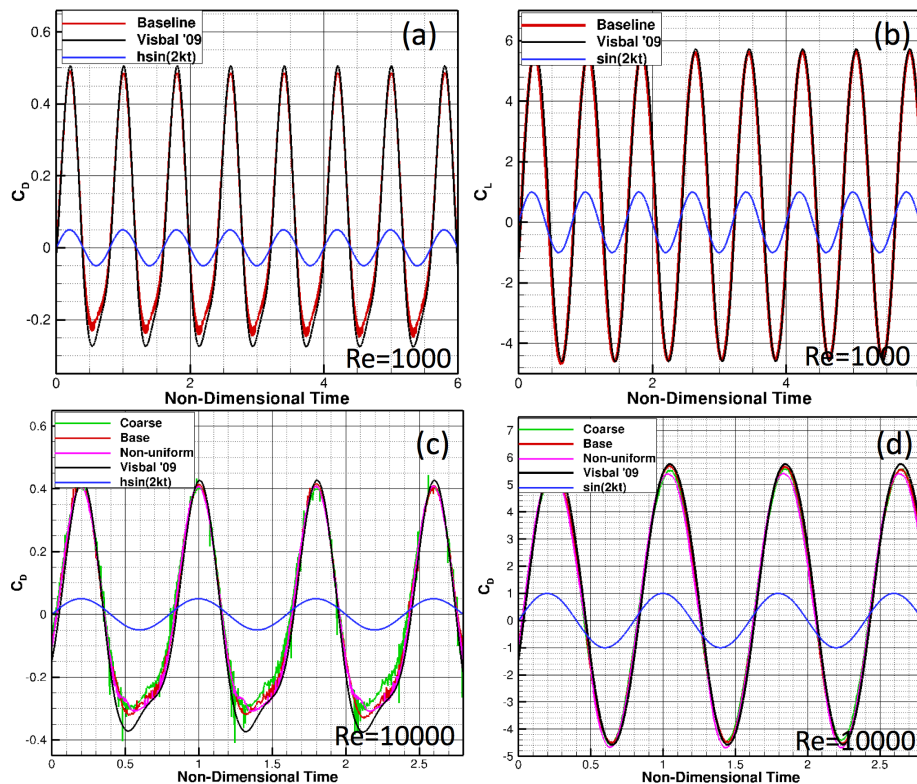

Figure 6. Two-dimensional loads on SD7003 airfoil at two different Reynolds numbers compared with the high-fidelity solver, FDL3DI:[2] (a,b) Drag and lift coefficients at $Re = 1000$, (c,d) drag and lift coefficients at $Re = 10000$. Predictions for baseline, coarse and non-uniform grids are shown.

American Institute of Aeronautics and Astronautics

length) for baseline and coarse grids, respectively. The corresponding resolutions along the airfoil surface were 0.005 and 0.01, respectively. For the present simulations, a baseline grid resolution of 0.00275×0.00275 was used in axial and vertical directions. The grids were cubical whereas those used by Visbal and co-workers were highly stretched in the wall-normal direction with very high aspect ratio. In the present study, a uniform coarse grid (twice as coarse compared to the baseline grid) was also used. In addition, non-cubic grids with much finer resolution in vertical direction compared to the axial direction were also used as shown in Table 1. Use of finer resolutions are feasible in the present solver; however, the simulations on thin, flat airfoil as planned in this study used similar resolutions as for the SD7003 case, in order to facilitate several parametric studies in reasonable time. The time-step used for the present incompressible flow simulations is also 4-times larger than those used by Visbal[2] in his compressible flow solver. The incompressible, pressure-based solver used in the present work allows for large time-steps (CFL ~ 0.2) with good accuracy without any numerical instabilities.

Figure 5 shows contour plots of out-of-plane vorticity at four different phase angles (plotted at midspan) for $Re = 10,000$ compared with corresponding plots by Visbal[2] showing very good qualitative comparison of the vortex structures on the baseline grid. The phases shown correspond to the positions of maximum upward displacement (Phase 0), maximum downward velocity (Phase 1/4), maximum downward displacement (Phase 1/2), and maximum upward velocity (Phase 3/4). Due to large effective angle of attack induced by the plunging motion during the downward stroke, leading edge separation occurs on the upper surface creating coherent dynamic-stall-like vortices. Two distinct leading-edge vortices are formed above the upper surface. Owing to high-frequency of plunging, these leading edge vortices travel close to the upper surface and prevent stall conditions. Due to the vortex-surface interaction, ejection of vorticity of opposite sign from the upper surface is also observed similar to the work by Visbal and co-workers. Formation of a single leading-edge vortex on the airfoil lower surface is also observed during the upstroke due to large negative angle of attack. All these features relate closely on the present baseline grid compared to those observed by Visbal and co-workers. Some deviations of vortex structures in the wake region are observed for the non-uniform or coarse grids; however, around the airfoil surface, all grids seem to provide similar flow structures. This is further confirmed by comparing the temporal evolution of lift and drag coefficients for $Re = 1000$ and $Re = 10,000$.

Quantitative comparison of the lift and drag coefficients were also obtained for $Re = 10^3, 10^4$ as shown in figure 6. It is seen that, for both Reynolds numbers the loads are well predicted. The drag coefficient is slightly under-predicted for $Re = 10000$, near the phase 3/4 of the periodic cycle. This may be attributed to the coarser wall-normal resolution in the present simulations compared to those by Visbal.[2] However, the asymmetric nature of the drag coefficient (especially for $Re = 10000$) is capture by present simulations. *This asymmetry actually results in mean thrust for these high-frequency plunging cases.* This case study also verifies the predictive capability of the present solver on grids comparable to those used in the thin airfoil study described below.

B. Flow Over Thin Flat Airfoil With and Without Leading Edge Actuation

Flow over a thin, flat airfoil at $Re = 14700$ and an angle of attack (α) of $20°$ is investigated. The chord length (c) is 20 cm, the thickness to chord ratio is 0.02, and the actuator length to chord ratio is 0.3. The airfoil has elliptical rounded edges with a height to length ratio of 1:5. In order to run simulations on an airfoil, first a computational model must be generated. Figure 3b shows the existing physical model.

The numerical model of the airfoil was created by distributing material points along the surface of the airfoil. The airfoil surface was defined by breaking the airfoil up into simpler shapes. The entire airfoil is generated at an angle of attack of zero with an actuator angle of zero. The material points are then rotated to the appropriate angle of attack. The five component shapes are an ellipse for the trailing edge, a line segment for the body of the airfoil, a semicircle for the hinge joint, a line segment for the flap body, and an ellipse for the leading edge. The origin for the airfoil is located at the trailing edge with the front of the airfoil pointed to the left (negative x direction). Due to the symmetry of the airfoil, for each point placed on the top surface of the airfoil, another is placed on the bottom surface by mirroring the top point across the x-axis. The airfoil is given depth by copying the points from the first cross-section to make additional cross-sections in the spanwise direction. The ellipses for the leading and trailing edges are generated using the following equation for an ellipse, the thickness of the airfoil, and the ratio of length to height:

$$\frac{(x - x_o)^2}{\frac{1}{2}rt_c^2} + y^2/t_c^2 = 1, \tag{4}$$

American Institute of Aeronautics and Astronautics

where x_o is the x location of the center of the ellipse, r is the length-to-height ratio (5 in this case) of the ellipse, and t_c is the thickness of the airfoil. The x locations of the material points are spaced evenly between the tip of the ellipse and the center. The y location is solved for using the above equation. The x_c for the trailing edge and leading edge are $(-t_c r/2)$ and $(t_c r/2c)$, respectively, where c is the chord length. Next the flat airfoil and actuator sections are added. Each flat section is generated by equally spacing material points along the flat surface. The airfoil flat surface extends from the end of the trailing edge ellipse to the start of the actuator hinge, and similarly, from the end of the actuator hinge to the end of the leading edge ellipse. Next the hinge material points are added. The hinge height and width are equal to the thickness of the airfoil. The hinge is formed by fitting two semi-circles into the gap between the airfoil surface and the flap surface. The semicircles are created tangent to both the flap and airfoil surfaces to create a smooth transition. The upper and lower semicircles are concentric. While adding the semi-circle to the underside of the airfoil does not match the shape of an actual hinge, the benefit is that the front actuator can be moved smoothly without the need to add material points. The final step is to rotate all the material points around the trailing edge by the specified angle of attack.

Grid resolutions used in the present calculations are given in Table 2. The baseline resolution is finer than that used for corresponding studies on the plunging SD7003 as discussed earlier. A coarse grid is also employed wherein, the grid resolution is coarsened in the streamwise direction. The effect of leading edge actuation is studied in two-steps: (i) static actuation; wherein, the leading edge actuator is held static at an angle relative to the angle of attack and altering the effective angle of attack, and (ii) dynamic actuation; wherein, the leading edge actuator is oscillated sinusoidally at different frequencies and amplitudes around a mean actuator position.

Table 2. Cartesian grid resolution and time-steps for thin, flat airfoil studies.

Grid	$\Delta x/c$	$\Delta y/c$	$\Delta t U_\infty/c$
Baseline	0.00166	0.00166	0.000125
Coarse (Non-Uniform)	0.005	0.00166	0.00025

1. Static Actuation Tests

As the first step, effect of the *static actuation* of the leading edge on the flowfield is investigated. The actuation angle (θ) (measured anti-clockwise from the axis of the airfoil) is set to $20°$, giving an effective angle of attack of $\alpha_\text{eff} = 13.77°$. This static actuation provides an effective camber to the airfoil and is expected to reduce flow separation and drag. Effect on the lift coefficient and mean lift-to-drag ratio are investigated. In order to provide a baseline case for aerodynamic load comparison, flow over a thin flat airfoil with no actuation (i.e. $\theta = 0°$) is considered in the numerical studies at $Re = 14700$. Obtaining experimental data at low Reynolds numbers is difficult in a wind-tunnel owing to small values of the drag and lift forces and thus increased uncertainty in their measurement. Maintaining constant low flow rate is also of concern. Hence, experimental data was collected at $Re = 42000$ and 70000 and different angles of attack and actuator angles. Table 3 compares the predicted lift coefficients for two different angles of attack and actuator angle set at $\theta = 10°$ with the experimental values. The comparison is reasonable and is within the uncertainty of the experimental measurement.

Table 3. Comparison of lift coefficients between present numerical and experimental studies for different angles of attack and actuator angle of $\theta = 10°$ at $Re = 70,000$.

Angle of Attack	C_L experimental	C_L numerical
$10°$	0.79	0.85
$14°$	1.06	1.16

Having established a baseline validation for aerodynamic loads on the thin, flat airfoil; the static actuation test was computed at lower Reynolds number of $Re = 14,700$. The effect of static actuation of the leading edge, with $\theta = 20°$ for an angle of attack (α) of $20°$, was first investigated. In this configuration, the leading edge remains horizontal and parallel to the incoming flow. The effective angle of attack is reduced to $13.77°$.

American Institute of Aeronautics and Astronautics

This allows the flow to develop on the leading edge and results in a smaller wake region. Figure 7 shows temporal evolution of out-of-plane vorticity contours for $\theta = 0°$ (no actuation) and $\theta = 20°$ (static actuation). With no actuation at an angle of attack of $20°$, highly separated and stalled flowfield is observed. The flow separates at the tip of the leading edge and the resultant vortices are convected downstream, parallel to the flow. A strong trailing edge vortex is also formed which interferes with the traveling vortex on the leading edge, giving rise to complex vortical flow features. When the leading edge is actuated in a static manner (i.e. $\theta = 20°$), the flow comes parallel to the leading edge. Flow separation is not as drastic as in the no actuation case. In this case, three distinct vortices are formed on the upper surface. These vortices travel very close to the upper surface, reducing the extent of the wake region. As the vortices pass the hinge region, they are thrown away from the surface and some vortex pairing is observed. These traveling vortices then interact with trailing edge vortex; however, remain fairly close to the upper surface of the wing.
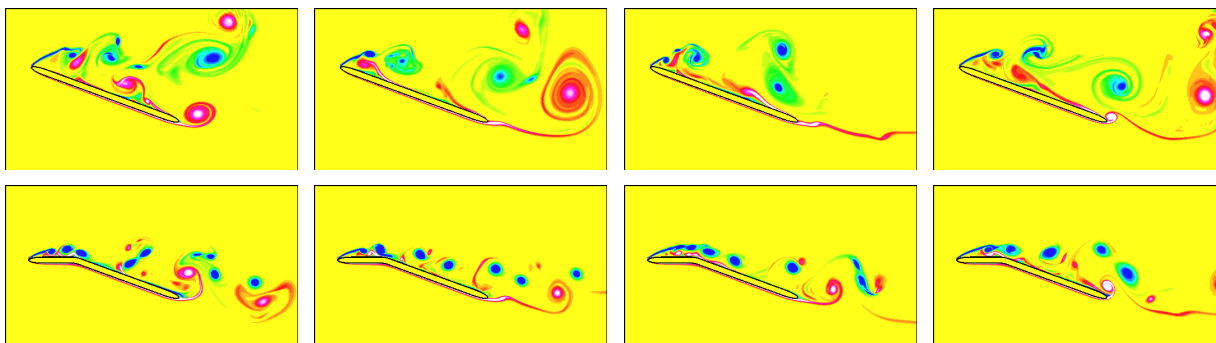

Figure 7. Effect of static actuation of the leading edge on flow structure as well as lift and drag for $\alpha = 20°$, $Re = 14700$. Top panel: out-of-plane vorticity contours ($\omega_z c/U_\infty = \pm 60$) for $\theta = 0°$, Bottom pannel: out-of-plane vorticity for $\theta = 20°$ (snapshots are $tU_\infty/c = 2.06$ apart).

Figure 8 shows the effect of static actuation on the aerodynamic loads. For no actuation, the lift and drag coefficients vary significantly for this high angle of attack, showing fluctuations due to passage of vortical structures past the leading edge. The flow is highly separated and stalled with a large wake region resulting large fluctuations in the aerodynamic loads. With simple static actuation, the magnitude of the mean drag coefficient is reduced (from 0.502 without actuation to 0.369 with actuation), whereas the mean lift coefficient is not altered significantly (from 1.03 without actuation to 0.97 with actuation). Also with static actuation, the range over which the lift and drag coefficients oscillate are reduced significantly. The mean lift-to-drag ratio is increased from 2.06 (without actuation) to 2.63 (with actuation), a 27.67% increase. However, both the lift and drag coefficients indicate rapid temporal variations due to passage of vortical structures and vortex-surface interactions. These results are obtained on the baseline grid, with similar levels of increase in mean lift-to-drag ratio shown by the coarse grid.

2. Dynamic Actuation Tests

Based on the static actuation of the leading edge, the effective angle of attack was altered which lowered the drag coefficient without significantly altering the lift coefficient. In addition, the extent of fluctuations in drag and lift coefficients were reduced significantly compared to no actuation. However, aerodynamic loads fluctuate rapidly in an uncontrolled manner. By flapping the leading edge actuator dynamically, it is hypothesized that the lift and drag coefficients can be varied in a more controlled manner. In order to investigate this, as the second step, sinusoidal actuation of the leading edge at different frequencies (1, 3, 5, 10, and 20 Hz), corresponding to the reduced frequencies of $k = \pi f c/U_\infty = 0.57$, 1.71, 2.86, 5.71, and 11.4, respectively, is performed.

For the SD7003 plunging case, it was observed that low amplitude, high frequency plunging motion results in a net negative drag (or thrust) owing to the plunging motion.[2] However, plunging the entire wing for a MAV is difficult in practice owing to high power requirements. In order to investigate if the more practical flapping motion of the leading edge actuator can result in net thrust, the airfoil was placed at zero angle of attack ($\alpha = 0°$), and the leading edge is flapped around the mean horizontal position at different frequencies and amplitudes.

Figure 9 shows the flow structure and evolution of the out-of-plane vorticity at different phase angles
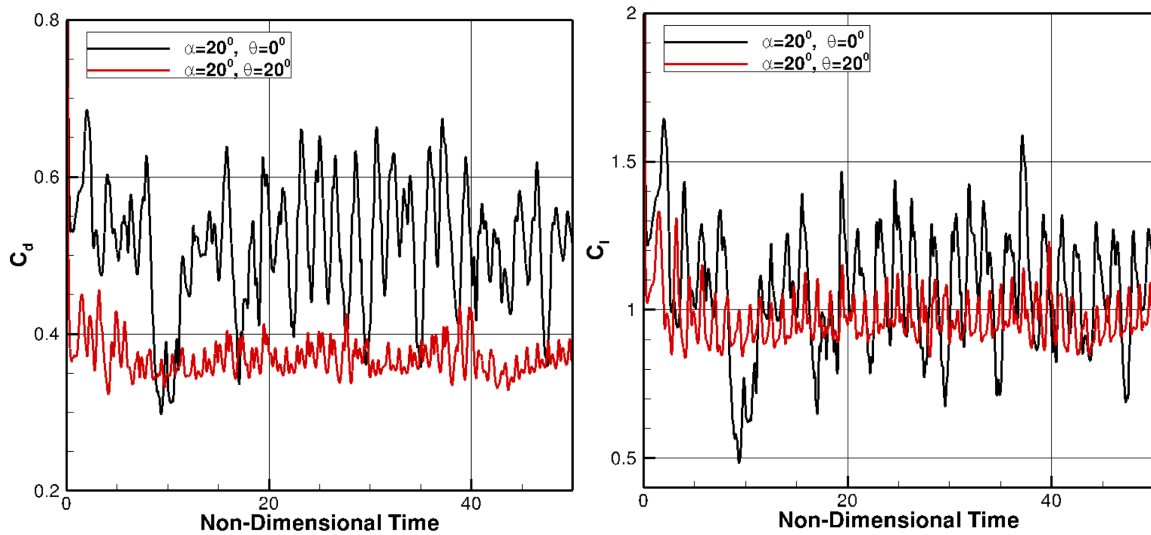
American Institute of Aeronautics and Astronautics

Figure 8. Effect of static actuation of the leading edge on aerodynamic loads for $\alpha = 20°$, $Re = 14700$. **Left panel: drag coefficient, right panel: lift coefficient. Black line (no actuation, $\theta = 0°$), red line (static actuation, $\theta = 20°$.)**
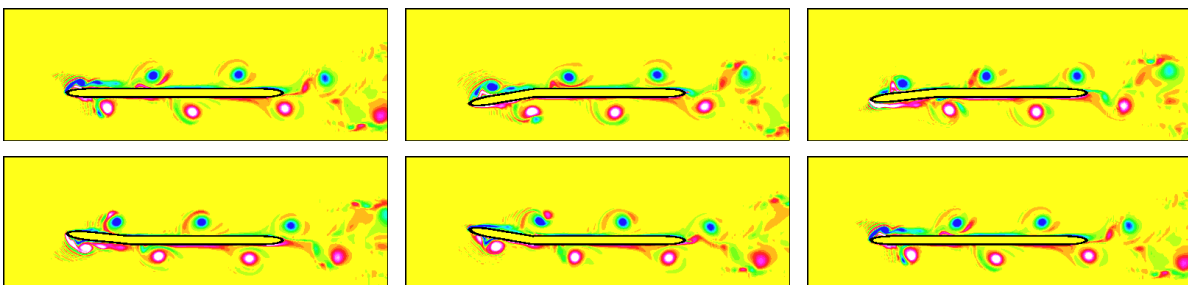

Figure 9. Out-of-plane vorticity contours ($\omega_z c/U_\infty = \pm 60$) showing effect of dynamic actuation of the leading edge on flow structure for $\alpha = 0°$, $Re = 14700$ and $\Delta\theta = \pm 10°$ at 10 Hz. **Top panel: Phase 0, Phase 1/5, Phase 2/5. Bottom panel: Phase 3/5, Phase 4/5, Phase 1.**

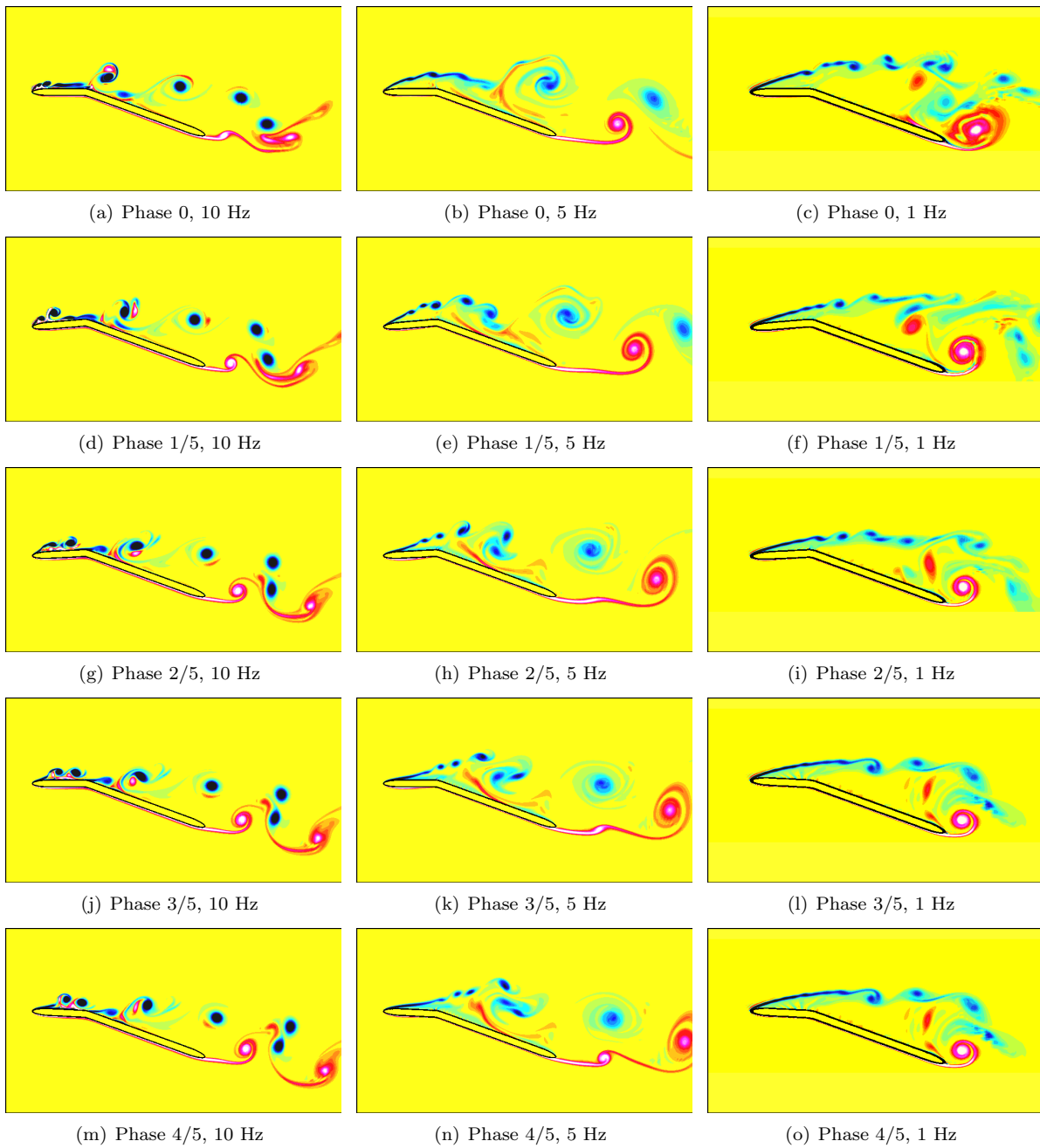(a) Phase 0, 10 Hz   (b) Phase 0, 5 Hz   (c) Phase 0, 1 Hz

(d) Phase 1/5, 10 Hz   (e) Phase 1/5, 5 Hz   (f) Phase 1/5, 1 Hz

(g) Phase 2/5, 10 Hz   (h) Phase 2/5, 5 Hz   (i) Phase 2/5, 1 Hz

(j) Phase 3/5, 10 Hz   (k) Phase 3/5, 5 Hz   (l) Phase 3/5, 1 Hz

(m) Phase 4/5, 10 Hz   (n) Phase 4/5, 5 Hz   (o) Phase 4/5, 1 Hz

Figure 10. Out-of-plane vorticity contours ($\omega_z c/U_\infty = \pm 60$) showing effect of dynamic actuation of the leading edge ($\Delta\theta = \pm 5°$) on flow structure for $\alpha = 20°$, $Re = 14700$. Left panel: 10 Hz ($k = 5.71$), middle panel: 5 Hz ($k = 2.86$), right panel: 1 Hz ($k = 0.57$) showing different phases of the actuation cycle.

American Institute of Aeronautics and Astronautics

for an actuation at 10 Hz and amplitude of $10°$ at $Re = 14700$. It is observed from the vorticity contours that the oscillatory actuation creates periodic vorticies which pass along the airfoil resulting in oscillatory variations in lift and drag coefficients. For the actuator length to chord ratio of 30%, it was found that the sinusoidal actuation resulted in a small net mean drag and also a positive mean lift. This study shows that the present actuation does not result in a mean thrust. A longer actuator may be necessary to obtain thrust; however, as shown later, this simple actuation can indeed provide increased mean lift-to-drag ratio at higher angles of attack. In addition, a predictable pattern for lift and drag variations is obtained.

Next, the angle of attack is kept at $\alpha = 20°$ and the mean actuator angle of $\theta = 20°$. In this configuration, the leading edge remains parallel to the flow direction. The actuator is sinusoidally oscillated about this mean position. The actuation frequency is varied from 1, 3, 5, 10, to 20 Hz. The actuation amplitudes are varied over range of ($\Delta\theta = 2.5°, 5°$, and $10°$). These vary the effective angles of attack over a wide range: $\alpha_{\mathrm{eff}} = 12.92 - 14.6°$, $12.04 - 15.4°$ and $10.2 - 17°$, respectively. The oscillatory actuations are about the mean actuator angle of $\theta = 20°$. Figure 10 shows the flow structure over one cycle of actuation for an amplitude of $\Delta\theta = \pm5°$ at three different frequencies. It is seen that for the high frequency of 10 Hz ($k = 5.71$), strong vortical structures created near the leading edge travel downstream. Vortex pairing mechanisms are observed with the vortices remaining close to the airfoil surface resulting in a smaller wake region. Downward motion of the leading edge leads to the formation of two strong leading edge vortices, very similar to the plunging SD7003 case studied earlier. These leading edge vortices travel downstream and as they come close to the hinge location, they are thrown away from the upper surface of the airfoil. It is also observed that, in addition to the creation of leading edge vortices, surface-vortex interaction leads to the ejection of vorticity of opposite sign. This ejected vorticity is prominent between the two leading-edge vortices, very similar to the high frequency plunging case of SD7003. Owing to the short cycle time (high frequency), new leading edge vortices are created before the old ones have chance to completely travel the chord length. Upward motion of the actuator creates a very weak vortex (unlike the plunging case of SD7003) on the bottom surface. These features result in increased mean lift-to-drag ratio as shown later.

For lower frequencies (5 and 1 Hz), the separated flow near the leading edge and the shear layer oscillate with the actuator motion. The flow remains separated over most of the cycle giving a larger wake, and the strong leading edge vortices observed in the high-frequency case are absent. With low frequency forcing, the vortex-surface interaction is not significant compared to the high frequency case. The ejection of opposite sign vorticity observed in high frequency case was absent for these frequencies.

Figure 11 shows the temporal variations of lift and drag coefficients for different frequencies and actuation amplitudes over a range of cycles. It is observed that for frequencies of 10 and 5 Hz, the lift/drag coefficients are periodic with a phase difference compared to the actuator motion. For large amplitude actuations ($10°$), the variations in lift and drag around a mean are also large. For lower frequencies of 1 Hz and also 3 Hz (not shown), the drag and lift coefficients oscillate, however, several periods appear superimposed. The fluctuations show similar characteristics as the static-actuation, especially for low frequency and low amplitude oscillations.

Tables 1–3 summarize the effect of static and dynamic actuation of the leading edge on the mean lift and drag coefficients for different actuation frequencies and amplitudes. Also compared are the mean lift-to-drag ratios to that obtained with no actuation. It is observed that any actuation (static or dynamic) results in an increase of mean lift-to-drag ratio compared to no actuation. With static actuation (i.e. $\theta = 20°$ for $\alpha = 20°$), an increase of 27.7% was observed. As shown in figure 8, the temporal variation of the lift and drag coefficients have a range of frequencies superimposed. With dynamic actuation at high frequencies (10 and 20 Hz) further increase in mean lift-to-drag ratios were observed. Specifically, for actuation amplitudes of $\Delta\theta = \pm5°$ and $\pm2.5°$ at high frequencies, an increase in mean lift-to-drag ratio of more than 50% was observed. In addition, for dynamic actuation, the temporal behavior of the lift and drag coefficients are periodic and predictable corresponding to the actuation frequency. With higher amplitudes of actuator motion, the range over which the lift and drag coefficients varied also increased. For lower frequencies (1, 3 and 5 Hz), the increase in mean lift-to-drag ratio is lower and the temporal variation in drag and lift coefficients show multiple frequencies superimposed similar to that observed in static actuation. These results suggest that high frequency actuation of the leading edge (either as designed or flow-induced) provide strong potential for development of control strategies. Specifically, these effects need to be investigated for airfoils undergoing transient maneuvers such as pitching or heaving.
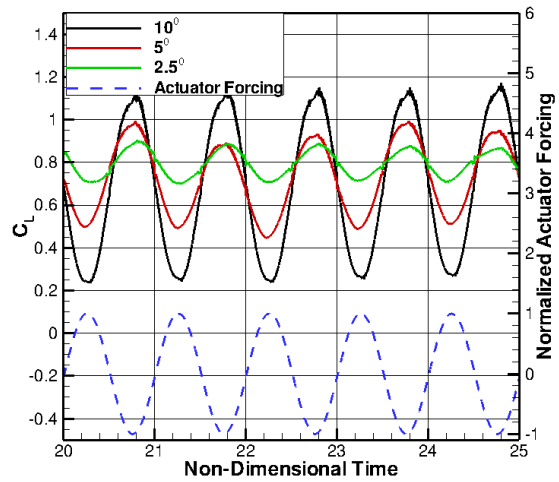
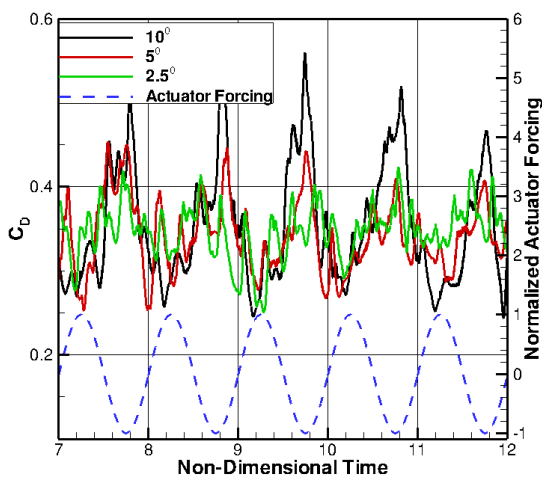American Institute of Aeronautics and Astronautics
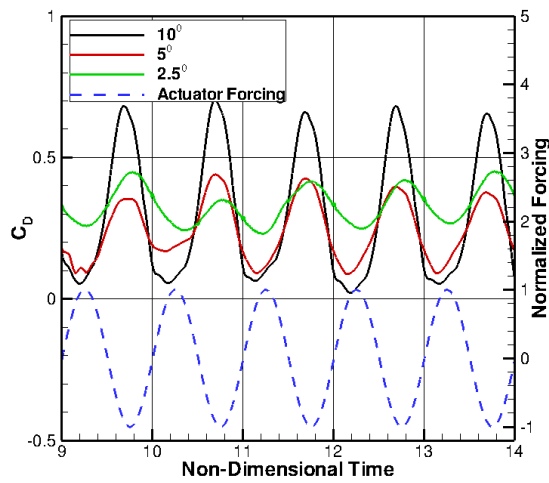
(a) C_D, 10 Hz
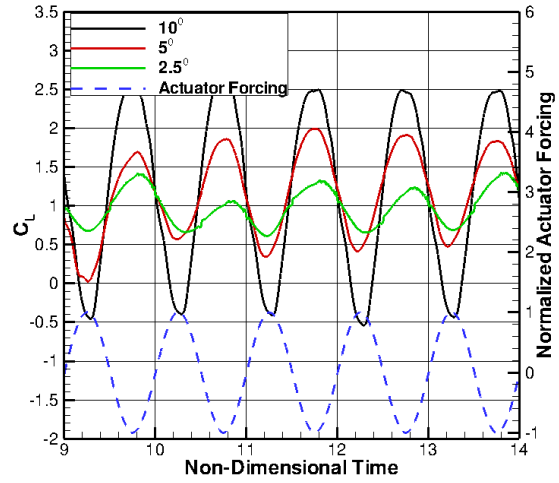
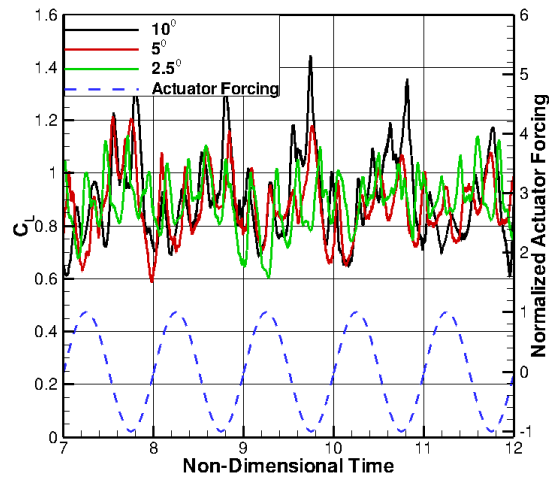(b) C_L, 10 Hz
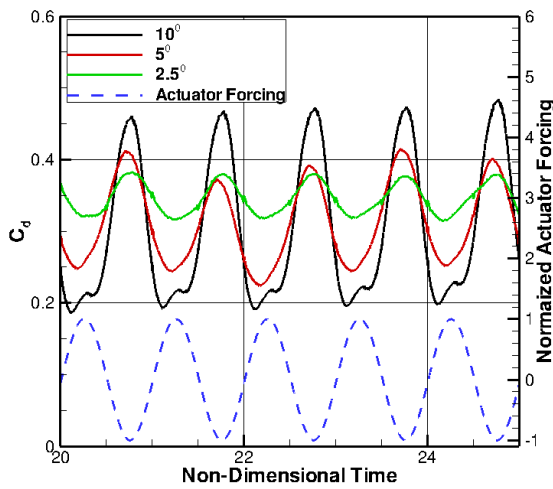
(c) C_D, 5 Hz

(d) C_L, 5 Hz

(e) C_D, 1 Hz

(f) C_L, 1 Hz

Figure 11. Temporal variation of drag and lift coefficients for different actuation amplitudes and frequencies at $Re = 14700$. Left panel: Drag Coefficients, Right Panel: Lift Coefficients. Also shown is the normalized actuator forcing.

American Institute of Aeronautics and Astronautics

Table 4. $\bar{C}_d$ and $\bar{C}_l$ for $Re_C = 14700$, $\Delta\theta = 10°$.

α_0	θ	frequency (reduced)	$\bar{C}_d$	$\bar{C}_l$	$\bar{C}_l/\bar{C}_d$	% increase
20°	0°	0	0.502	1.034	2.06	-
20°	20°	0	0.369	0.97	2.63	27.7%
20°	20°	10 Hz (5.71)	0.281	1.11	3.96	91.75%
20°	20°	5 Hz (2.86)	0.32	0.75	2.35	13.75%
20°	20°	1 Hz (0.571)	0.34	0.85	2.5	21.3%

Table 5. $\bar{C}_d$ and $\bar{C}_l$ for $Re = 14700$, $\Delta\theta = 5°$.

α_0	θ	frequency (reduced)	$\bar{C}_d$	$\bar{C}_l$	$\bar{C}_l/\bar{C}_d$	% increase
20°	20°	20 Hz (11.42)	0.36	1.06	2.94	43%
20°	20°	10 Hz (5.71)	0.224	1.12	5	142%
20°	20°	5 Hz (2.86)	0.31	0.76	2.45	19%
20°	20°	1 Hz (0.571)	0.34	0.89	2.61	22.78%

Table 6. $\bar{C}_d$ and $\bar{C}_l$ for $Re = 14700$, $\Delta\theta = 2.5°$.

α_0	θ	frequency (reduced)	$\bar{C}_d$	$\bar{C}_l$	$\bar{C}_l/\bar{C}_d$	% increase
20°	20°	20 Hz (11.42)	0.3066	1.025	3.34	62.2%
20°	20°	10 Hz (5.71)	0.30	0.934	3.11	51.1%
20°	20°	5 Hz (2.86)	0.35	0.795	2.27	10.26%

C. Experimental Data at Higher Reynolds Number ($Re = 42,000$)

The experimental cases are presented to illustrate the effects of leading edge actuation at $Re = 42,000$ with an actuator angle range equivalent to a range of effective angle of attack of 12.04-15.40 ($\pm 5°$) with three reduced frequencies of 1.14, 1.71 and 2.86 (2, 3 and 5 Hz, respectively). Note that the data have all been low pass filtered at 12 Hz to facilitate observation of how the large amplitude oscillations vary and how they are related to the actuator oscillations in terms of phase. It should also be noted that, the flow Reynolds number is roughly three-times higher than that studied with DNS. Accordingly, the inlet velocity is three times higher (3 m/s), and convective time scales of advection of vortices over the airfoil will be roughly three-times lower. This also means that lower actuator frequencies (2-5 Hz) can still show significant influence on the drag and lift characteristics at this higher Re, than as observed in DNS at lower $Re = 14700$.

The lowest frequency results, $k = 1.14$, are shown in figure 12a,b for both C_D and C_L. For these results, and for the other experimental data, the actuator forcing function is shown on the figures as a sine wave. The lift and drag force time traces are shown in nondimensional time in relation to the actuator time trace. The actuator forcing function is such that its peak value corresponds to the maximum downward position, or $\alpha_{\text{eff}} = 12.04°$. The minimum corresponds to the minimum downward position with $\alpha_{\text{eff}} = 15.40°$. The first item of interest is the slight phase shift of the peak value of both C_L and C_D. Note that the peak values occur slightly after the minimum downward position (largest α_{eff}). Similarly, this phase shift occurs for the minima of C_L and C_D relative to the minima of α_{eff}. Similar phase shift in drag and lift coefficients was observed in DNS at lower Re. A second feature to note is that the higher frequency events that occur near the maxima and minima of both C_L and C_D are believed to be a result of the directional change of the actuator and occur at both the maxima and minima with approximately the same amplitude.

At the intermediate frequency, $k = 1.71$ shown in figure 12c,d, a similar phase shift occurs as seen at the lower frequency. There is still evidence of the higher frequency effects near the maxima and minima, however, they are much less pronounced. When going to the highest frequency studied, $k = 2.86$, shown in figure 12e,f, the maxima higher frequency events remain, but interestingly the minima events seem to be essentially eliminated.

Overall, for all three frequencies studied, the results demonstrate the strong phase relationship to the leading edge actuator. The major amplitude changes coincide with the actuator resulting in peaks of C_L and C_D coinciding with the largest value of α_{eff} (which results in the highest instantaneous camber). However, during directional changes of the actuator very discrete higher frequency events occur. This is suspected
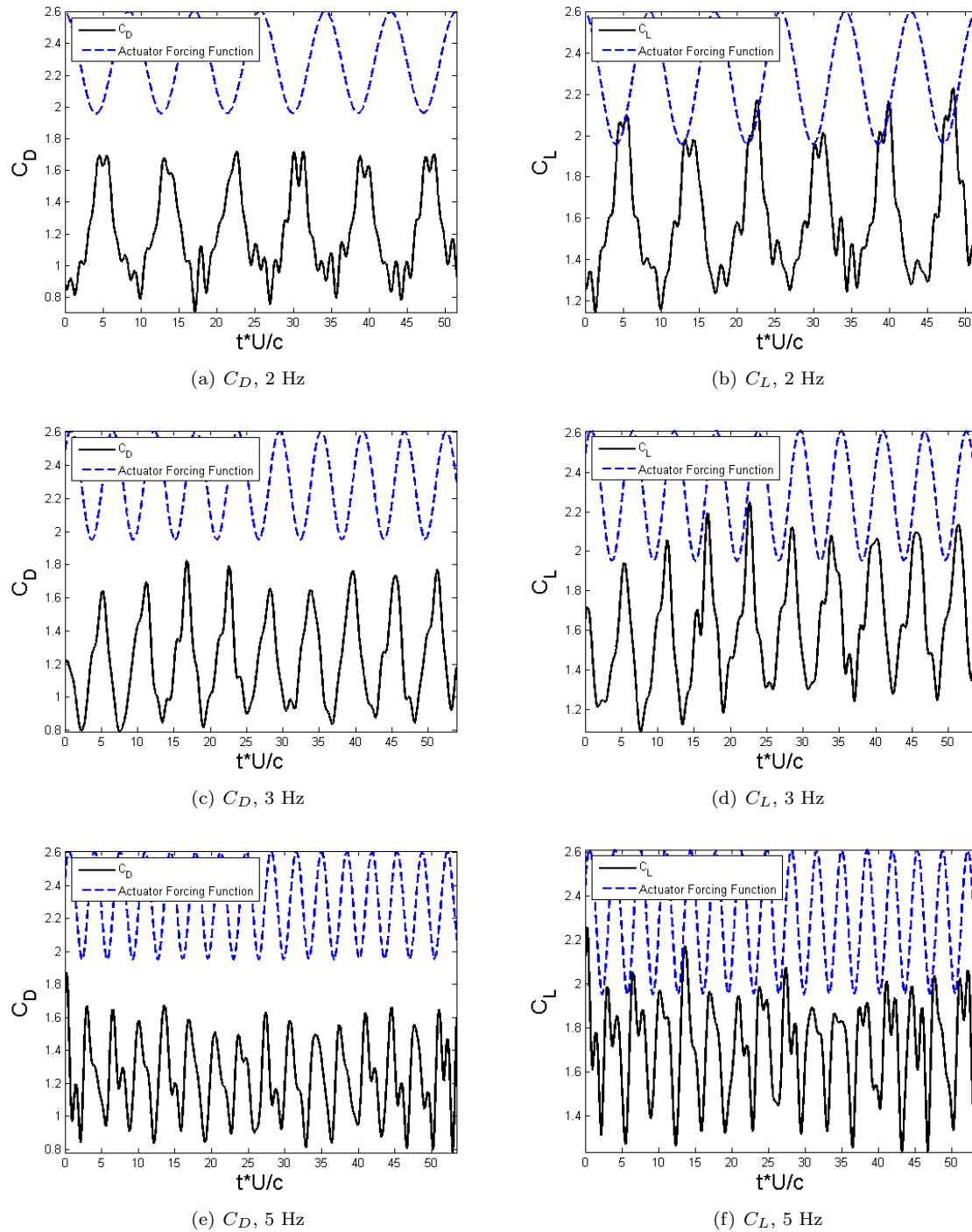
American Institute of Aeronautics and Astronautics

(a) C_D, 2 Hz

(b) C_L, 2 Hz

(c) C_D, 3 Hz

(d) C_L, 3 Hz

(e) C_D, 5 Hz

(f) C_L, 5 Hz

Figure 12. Experimental data showing temporal variation of drag and lift coefficients for $\alpha = 20°$, $\theta = 20°$, $\Delta\theta = \pm 5°$ at $Re = 42000$ and different actuator frequencies.

to be associated with vortex generation and convection along the surface, which then in turn affects the instantaneous lift and drag. At the lowest frequency the fluctuations during the highest α_{eff} are most significant. These are no longer seen at the higher frequency.

Consequently, one may conclude that the lower frequency actuation near the minima of α_{eff} results in more dominant generated vortices that convect along the actuator. It is speculated that at higher frequencies these vortices are not as strong, due to more rapid transition through the directional change of the actuator and consequently do not appear to influence the measured instantaneous lift and drag.

V.   Summary and Conclusion

Effect of oscillatory actuation of the leading edge of a thin, flat, rigid airfoil on MAV performance was investigated using two-dimensional simulations at low Reynolds number of 14700 and experimental data at $Re = 42000$ and $20°$ angle of attack. A second-order accurate, fictitious domain method was used for this moving boundary problem on a fixed background mesh. The numerical method was thoroughly verified for its accuracy and predictive capability on canonical problems of flow over a cylinder and sphere at different Reynolds numbers, flow over a NACA hydrofoil, flow generated by an inline oscillation of the cylinder and flow over a plunging SD7003 airfoil. Good comparison was obtained for plunging studies of SD7003 airfoil compared to AFRLs high-fidelity solver FDL3DI for Reynolds numbers of 10^3 and 10^4.

Flow over a thin, flat airfoil at high angle of attack was studied with and without actuation of the leading edge. Leading edge actuation involving rotation around a hinge located at 30% chord length can be used to reduce the effective angle of attack without significantly reducing the lift. Reduction in effective angle of attack and the added camber, results in reduced drag. A 27% increase in mean lift-to-drag ratio was observed for static actuation cases, wherein the leading edge flap was horizontal ($\theta = 20°$). Actuated leading edge at different reduced frequencies (0.57-11.42) and amplitudes ($2.5°$ -$10°$) were also studied. It was observed that high frequency actuation of $10, 20$ Hz ($k = 5.71, 11.42$), further increases the mean lift-to-drag ratio ($> 50\%$). It also provides predictable pattern of lift and drag variations. Further analysis to study effect on mean flow/pressure, accounting for three-dimensional, transition effects as well as experimental data are needed to corroborate these findings.

The present work indicated that the leading edge actuation using a hinged flapping actuator provides a means to directly influence the leading edge stall condition and unsteady lift behavior while not adding complexities associated with blowing or suction that may not be practical, for small wings with weight constraints. Control strategies based on the present leading edge actuation are of direct relevance to small-size MAVs undergoing maneuvers and are pragmatic as designing simple piezo-based actuators is straightforward. The present simple modification to the wing configuration also facilitates development of actuators and controllers for airfoils with considerable size and weight restrictions. For instance, typical characteristic lengths for MAV are in the range of 8–15 cm, with operating speeds on the order of 50 km/h. Improving the flight performance of these vehicles can enhance surveillance, search and rescue, and sensor mobility, while yielding vehicles that are more disposable.

Although this work investigated rigid airfoils, the results are of direct relevance to other forms of leading edge flow control which are more amenable to small scale MAV implementation; for example, surface deformations via piezo-electric actuators or aero-elastically tailored structures. In addition, concepts of passive control, with spring mounted hinge are also feasible leading to flow-induced actuation of the leading edge. By designing spring constants that result in flow-induced actuator motion that is periodic may result in added advantage of increased lift-to-drag ratio without any need to supply power for actuator motion.

Acknowledgments

American Institute of Aeronautics and Astronautics

References

[1]Visbal, M., "High-fidelity simulation of transitional flows past a plunging airfoil," *AIAA paper*, Vol. 391, 2009, pp. 2009.

[2]Visbal, M., Gordnier, R., and Galbraith, M., "High-fidelity simulations of moving and flexible airfoils at low Reynolds numbers," *Experiments in Fluids*, Vol. 46, No. 5, 2009, pp. 903–922.

[3]Apte, S., Martin, M., and Patankar, N., "A numerical method for fully resolved simulation (FRS) of rigid particle-flow interactions in complex flows," *Journal of Computational Physics*, 2008, pp. doi:10.1016/j.jcp.2008.11.034.

[4]Moin, P. and Apte, S., "Large eddy simulation of multiphase reacting flows in complex combustors," *AIAA J. (special issue on 'Combustion Modeling and LES: Development and Validation Needs for Gas Turbine Combustors)*, Vol. 44, 2006, pp. 698–710.

[5]Hoarau, Y., Braza, M., Ventikos, Y., Faghani, D., and Tzabiras, G., "Organized modes and the three dimensional transition to turbulence in the incompressible flow around a NACA0012 wing," *J. Fluid Mech.*, Vol. 496, 2003, pp. 63–72.

[6]Nishimura, H. and Taniike, Y., "Aerodynamic characteristics of fluctuating forces on a circular cylinder," *J. Wind Eng., Ind. Aerodynamics*, Vol. 89, 2001, pp. 713–723.

[7]Sicot, C., Auburn, S., Loyer, S., and Devinant, P., "Unsteady characteristics of the static stall of an airfoil sujected to freestream turbulence level up to 16%," *Exp. in Fluids*, Vol. 41, 2006, pp. 641–648.

[8]Fabula, A., "This airfoil theory applied to hydrofoils with a single finite cavity and arbitrary free-streamline detatchment," *J. Fluid Mech.*, Vol. 12, 1962, pp. 227–240.

[9]Kao, H., "Some aspects of airfoil stall in low speed flow," *J. Aircraft*, Vol. 11, No. 3, 1974, pp. 177–180.

[10]Atik, H., Kim, C., van Dommelen, L., and Walker, J., "Boundary-layer separation control on a thin airfoil using local suction," *J. Fluid Mech.*, Vol. 535, 2005, pp. 414–443.

[11]Degani, A., Li, Q., and Walker, J., "Unsteady separation from teh leading edge of a thin airfoil," *Phy. Fluids*, Vol. 8, No. 3, 1996, pp. 704–714.

[12]Zaitsev, O. and Sychev, V., "Steady flow with separation past a thin airfoil at high Reynolds numbers," *J. Fluid Dynamics*, Vol. 29, No. 2, 1994, pp. 277–281.

[13]Simpson, R., Chew, Y., and Shivaprasad, B., "The structure of a separating turbulent boundary layer: Part I, mean flow and Reynolds stresses and Part II, higher order turbulence results," *J. Fluid Mech.*, Vol. 113, 1981, pp. 23–73.

[14]Min and Choi, H., "Suboptimal feedback control of vortex shedding at low Reynolds numbers," *J. Fluid Mech.*, Vol. 401, 1999, pp. 123–156.

[15]Cheng, M. and Chen, B., "A numerical study on fluid forced reduction of a square cylinder by flow control," *FEDSM2007-37025, Proc. FEDSM2007, Joint ASME/JSME Fluids Engineering Conf., San Diego, CA*, 2007.

[16]McManus, K. and Magill, J., "Separation control in incompressible and compressible flows using pulsed jets," *AIAA 96-1948, AIAA Fluids Dyn. Conf., New Orleans, LA*, 1996.

[17]Florent, R., Pascal, M., and Didier, B., "Experimental control of vortex breakdown by pulsed blowing over a delta wing with rounded leading-edge," *FEDSM2002-31039, Proc. of ASME FEDSM2002, Montreal, CA*, 2002.

[18]Gallas, Q., Holman, R., Nishida, T., Carroll, B., Sheplak, M., and Cattafesta, L., "Lumped element modeling of piezoelectric-driven synthetic jets," *AIAA J.*, Vol. 41, 2003, pp. 240–247.

[19]Baysal, O., Koklu, M., and Erbas, N., "Design optimization of micro synthetic jet acutators for flow separation control," *J. Fluids Eng.*, Vol. 128, 2006, pp. 1053–1062.

[20]Scholz, P., Ortmanns, J., Kahler, C., and Radespiel, R., "Leading edge separation control by means of pulsed jet actuators," *3rd AIAA Flow Cont. Conf., 2006-2000*, 2006.

[21]Corke, T., Enloe, C., and Wilkinson, S., "Dielectric Barrier Discharge Plasma Actuators for Flow Control*," *Annual Review of Fluid Mechanics*, Vol. 42, 2010, pp. 505–529.

[22]Visbal, M., Gaitonde, D., and Roy, S., "Control of transitional and turbulent flows using plasma-based actuators," *AIAA paper*, Vol. 3230, 2006, pp. 2006.

[23]Grundmann, S. and Tropea, C., "Experimental transition delay using glow-discharge plasma actuators," *Experiments in fluids*, Vol. 42, No. 4, 2007, pp. 653–657.

[24]Gang, L., Chaoqun, N., Yiming, L., Junqiang, Z., and Yanji, X., "Experimental Investigation of Flow Separation Control Using Dielectric Barrier Discharge Plasma Actuators," *Plasma Science and Technology*, Vol. 10, 2008, pp. 605.

[25]Dong, B., Bauchire, J., Pouvesle, J., Magnier, P., and Hong, D., "Experimental study of a DBD surface discharge for the active control of subsonic airflow," *Journal of Physics D: Applied Physics*, Vol. 41, 2008, pp. 155201.

[26]Rizzetta, D. and Visbal, M., "Numerical Investigation of Plasma-Based Control for Low-Reynolds Number Airfoil Flows," *AIAA Paper 2010-4255, 5th AIAA Flow Control Conference, Chicago, IL*.

[27]Brunton, S., Rowley, C., Taira, K., Colonius, T., Collins, J., and Williams, D., "Unsteady aerodynamic forces on small-scale wings: experiments, simulations and models," *46 th AIAA Aerospace Sciences Meeting and Exhibit*, American Institute of Aeronautics and Astronautics, 1801 Alexander Bell Drive, Suite 500, Reston, VA, 20191-4344, USA,, 2008.

[28]Geissler, W., Sobieczky, H., and Vollmers, H., "Numerical study of the unsteady flow on a pitching airfoil with oscillating flap," *European Rotorcraft Forum, 24 th, Marseilles, France*, 1998.

[29]Lu, Y., Shen, G., and Lai, G., "Dual leading-edge vortices on flapping wings," *Journal of Experimental Biology*, Vol. 209, No. 24, 2006, pp. 5005.

[30]Muijres, F., Johansson, L., Barfield, R., Wolf, M., Spedding, G., and Hedenstrom, A., "Leading-edge vortex improves lift in slow-flying bats," *Science*, Vol. 319, No. 5867, 2008, pp. 1250.

[31]Dickinson, M., Lehmann, F., and Sane, S., "Wing rotation and the aerodynamic basis of insect flight," *Science*, Vol. 284, No. 5422, 1999, pp. 1954.

[32]Taira, K., Dickson, W., Colonius, T., Dickinson, M., and Rowley, C., "Unsteadiness in flow over a flat plate at angle-of-attack at low Reynolds numbers," *45 th Aerospace Sciences Meeting and Exhibit, AIAA,(AIAA 2007-710)*.

[33]Taira, K. and Colonius, T., "Three-dimensional flows around low-aspect-ratio flat-plate wings at low Reynolds numbers," *Journal of Fluid Mechanics*, Vol. 623, 2009.

[34]Colonius, T., Rowley, C., Tadmor, G., Williams, D., Taira, K., Dickson, W., Gharib, M., and Dickinson, M., "Closed-loop control of leading-edge and tip vortices for small UAV," *Conference on Active Flow Control*, 2006.

[35]Ol, M., McAuliffe, B., Hanff, E., Scholz, U., and Kaehler, C., "Comparison of laminar separation bubble measurements on a low Reynolds number airfoil in three facilities," *AIAA paper*, Vol. 5149, 2005, pp. 2005.

[36]Radespiel, R., Windte, J., and Scholz, U., "Numerical and experimental flow analysis of moving airfoils with laminar separation bubbles," *AIAA journal*, Vol. 45, No. 6, 2007, pp. 1346.

[37]McGowan, G., Gopalarathnam, A., Ol, M., Edwards, J., and Fredberg, D., "Computation vs. experiment for high-frequency low-reynolds number airfoil pitch and plunge," *AIAA*, Vol. 653, 2008, pp. 2008.

[38]Sahoo, D., Srinivasan, R., and Bowersox, R., "Examination of the Leading Edge Flow Structure of a Dynamically Pitching NACA 0012 Airfoil," *47 th AIAA Aerospace Sciences Meeting Including the New Horizons Forum and Aerospace Exposition(Disc 1)*, American Institute of Aeronautics and Astronautics, 1801 Alexander Bell Drive, Suite 500, Reston, VA, 20191-4344, USA,, 2009.

[39]Mueller, T. and DeLaurier, J., "An overview of micro air vehicle aerodynamics.' Fixed and flapping wing aerodynamics for micro air vehicle applications," *Progress in Astronautics and Aeronautics*, Vol. 195, 2001, pp. 1–10.

[40]Pelletier, A. and Mueller, T., "Low Reynolds number aerodynamics of low-aspect ratio, thin/flat/cambered-plate wings," *J. of Aircraft*, Vol. 37, No. 5, 2000, pp. 825–832.

[41]Broeren, A. and Bragg, M., "Unsteady stalling characteristics of thin airfoils at low Reynolds numbers. Fixed and flapping wing aerodynamics for micro air vehicle applications," *Progress in Astronautics and Aeronautics*, Vol. 195, 2001, pp. 191–213.

[42]Yarusevych, S., Sullivan, P., and Kawall, J., "Airfoil boundary layer separation and control at low Reynolds numbers," *Exp. Fluids*, Vol. 38, 2005, pp. 545–547.

[43]Fuchiwaka, M., Tanaka, K., and Nakashima, M., "Characteristics of dynamic thrust on an unsteady airfoil in pitching and heaving motions," *FEDSM2007-37222, Proc. FEDSM20007, Joint ASME/JSME Fluids Engineering Conf., San Diego, CA*, 2007.

[44]Selig, M. and Guglielmo, J., "High lift low Reynolds number airfoil design," *J. of Aircraft*, Vol. 34, No. 1, 1997, pp. 72–79.

[45]Shyy, W., Klevebring, F., Nilsson, M., Sloan, J., Carroll, B., and Fuentes, C., "Rigid and flexible low Reynolds number airfoils," *J. of Aircraft*, Vol. 36, No. 3, 1999, pp. 523–529.

[46]Gopalarathnam, A., Broughton, B., McGrananhan, B., and Selig, M., "Design of low Reynolds number airfoils with trips," *J. of Aircraft*, Vol. 40, No. 4, 2003, pp. 768–775.

[47]Kunz, P. and Kroo, I., "Analysis and design of airfoils for use at ultra-low Reynolds numbers. Fixed and flapping wing aerodynamics for micro air vehicle applications," *Progress in Astronautics and Aeronautics*, Vol. 195, 2001, pp. 35–60.

[48]Apte, S. and Finn, J., "A variable density fictitious domain method for fully resolved simulation of high-density ratio fluid-particle systems," *ICMF2010, Seventh International Conference on Multiphase Flow, Tampa Bay, FL*.

[49]Mahesh, K., Constantinescu, G., and Moin, P., "A new time-accurate finite-volume fractional-step algorithm for prediction of turbulent flows on unstructured hybrid meshes," *J. Comp. Phy.*, Vol. 197, 2004, pp. 215–240.

[50]Apte, S. and Patankar, N., "A formulation for fully resolved simulation (FRS) of particle–turbulence interactions in two-phase flows," *International Journal of Numerical Analysis and Modeling*, Vol. 5, Suppl, 2008, pp. 1–16.

[51]Morse, D. R. and Liburdy, J. A., "Vortex Dynamics and Shedding of a Low Aspect Ratio, Flat Wing at Low Reynolds Numbers and High Angles of Attack," *Journal of Fluids Engineering*, Vol. 131, No. 5, 2009, pp. 051202.

[52]Morse, D. and Liburdy, J., "Dynamic characteristics of flow separation from a low Reynolds number airfoil," *FEDSM2007-37083, Fluids Eng. Conf, San Diego, CA.*, 2007.

[53]Morse, D. and Liburdy, J. A., "Vortex detection and characterization in low Reynolds number separation," *IMECE2007-43011, ASME Int. Mech. Eng. Cong. & Exp., Seattle, WA*, 2007b.

[54]Chen, G., Lin, Z., Morse, D., Snider, S., Apte, S., Liburdy, J., and Zhang, E., "Multiscale feature detection in unsteady separated flows," *International Journal of Numerical Analysis and Modeling*, Vol. 5, 2008, pp. 1–16.

[55]Morse, D., Snider, S., Chen, G., Apte, S., Liburdy, J., and Zhang, E., "Detection and Analysis of Separated Flow Induced Vortical Structures," *to appear in 46th AIAA Aerospace Sciences Meeting and Exhibit, Reno, NV*, January 2008.